Aalborg Universitet

AALBORG UNIVERSITY
DENMARK

Two-dimensional thermal analysis of radial heat transfer of monoliths in small-scale steam methane reforming

Cui, Xiaoti; Kær, Søren Knudsen

Two-dimensional thermal analysis of radial heat transfer of monoliths in small-scale steam methane reforming

Xiaoti Cui, Søren Knudsen Kær

Department of Energy Technology, Aalborg University

Pontoppidanstr. 111

9220 Aalborg

E-mail: xcu@et.aau.dk

Phone: +45 2667 8192

Abstract

Monolithic catalysts have received increasing attention for application in the small-scale steam methane reforming process. The radial heat transfer behaviors of monolith reformers were analyzed by two-dimensional computational fluid dynamic (CFD) modeling. A parameter study was conducted by a large number of simulations focusing on the thermal conductivity of the monolith substrate, washcoat layer, wall gap, radiation heat transfer and the geometric parameters (cell density, porosity and diameter of monolith). The effective radial thermal conductivity of the monolith structure, $k_{r,eff}$, showed good agreement with predictions made by the pseudo-continuous symmetric model. This influence of the radiation heat transfer is low for highly conductive monoliths. A simplified model has been developed to evaluate the importance of radiation for monolithic reformers under different conditions. A wall gap as thin as 0.05 mm significantly decreased $k_{r,eff}$, while the radiation heat transfer showed limited improvement. A pseudo-homogenous two-dimensional model combined with the symmetric model has been developed for a quick evaluation of geometric parameters for a monolith reformers. Monolithic reformers based on highly conductive substrates e.g., Ni and SiC showed great potential for small-scale hydrogen production.

Keywords:

- Thermal analysis;

- Radiation;

- Monolith;

- Computational fluid dynamics;

- Steam methane reforming;

- Endothermic reaction;

Nomenclature

a	(-)	Adsorption coefficient
Cd	cells/cm^2	Cell density of monolith structure
d	m	Diameter of monolith; side length of square channel
E	J/mole	Activation energy
F_{kj}	(-)	View factor
f	(-)	Enhancement factor of radiation heat transfer
f_{wash}	(-)	Influence of washcoat layer on the G factor
G	(-)	Factor for evaluate the effective thermal conductivity
G_{rad}	(-)	G factor considering radiation heat transfer
G_{gap}	(-)	G factor considering the wall gap
$G_{gap,rad}$	(-)	G factor considering radiation and the wall gap
ΔT	K	Temperature difference T_w - T_c
ΔT_m	K	ΔT value for monolith structure
ΔT_s	K	ΔT value for solid structure
ΔT	K	Temperature difference
k	W/m·K	Thermal conductivity
$k_{CH4,T}$	mole·m^{-3}·s^{-1}·bar^{-1}	Reaction constant
k_f	W/m·K	Thermal conductivity of gas phase
k_s	W/m·K	Thermal conductivity of monolith substrate
$k_{r,eff}$	W/m·K	Effective radial thermal conductivity
$k_{r,eff,gap}$	W/m·K	Effective radial thermal conductivity considering the wall gap
k_w	W/m·K	Thermal conductivity of washcoat
n	(-)	refractive index
P_{CH4}	bar	Partial pressure of CH_4
q	W/m^2	Heat flux
$q_{out,k}$	W/m^2	Energy fluxes leaving surface k
Q_m	W	Total heat transfer rate through monolith structure
$Q_{mono,avg}$	W/m^3	Average reaction heat for the bulk monolithic bed
Q_s	W	Total heat transfer rate through pure solid
Q_{wash}	W/m^3	Reaction heat in the washcoat
$Q_{wash,ref}$	W/m^3	Reference reaction heat in the washcoat
R_{wash}	mole·m^{-3}·s^{-1}	Reaction rate
R	J·mole^{-1}·K^{-1}	Gas constant
S_{ch}	m^2	Surface area of the monolith channels
S_R	W/m^3	Volumetric heat source
T	K	Temperature
T_c	K	Temperature at the center
T_{ref}	K	Reference temperature
T_w	K	Temperature at the outer wall
V_{mono}	m^3	Monolith volume
W	m	Overall cell dimension

Greek letters

δ_{wash}	μm	Washcoat thickness
δ'_{wash}	μm	Virtual washcoat thickness
ε	(-)	Porosity of a bare monolith without washcoat layer; emissivity of channel surface
ε_k	(-)	Emissivity of surface k
λ	μm	Thermal conductivity
ξ	(-)	Volume fraction of washcoat
ρ_k	(-)	Refractivity of surface k
σ	W/m^2·K^4	Stefan-Boltzmann constant
φ	(-)	Volume fraction of the gas phase

Subscripts

avg	average
c	Center
ch	Monolith channel
CH$_4$	Methane gas
f	Gas phase
gap	Wall gap
k	Surface k,
m	monolith
mono	monolith
rad	Radiation heat transfer
ref	reference
s	Solid; monolith substrate
w	Outer wall; washcoat
wash	washcoat

1. Introduction

Steam methane reforming (SMR) is well-established method and is currently the preferred route for large-scale hydrogen production which is used as the raw material for the production of ammonia and methanol and for hydrotreating in refineries [1, 2]. For the distributed generation of hydrogen on a smaller scale (e.g., for hydrogen fueling stations), SMR is also economically attractive since it takes advantage of the existing natural gas supply infrastructure [3]. More attentions have been paid to the study on small-scale SMR reformers for hydrogen production in the power system (combined with fuel cells) for commercial and residential application [4–7].

Unlike large-scale SMR, small-scale SMR requires a smaller and more compact reformer in cramped conditions with limited space (e.g., for the use of micro-combined heat and power systems in a home) and a quick response for frequent start-up, shut-down, and transient operations [8–9]. These requirements can be better fulfilled by structured reactors such as monolith reactors than by fixed-bed reactors, which are typically applied to large-scale SMR [10]. Monolith reactors have been successfully used in environmental applications, especially for the treatment of exhaust gas in automobiles. In recent years, these reactors have gained more interests due to their potential applications in fuel processing, such as steam reforming of hydrocarbons for small-scale hydrogen production [10–11].
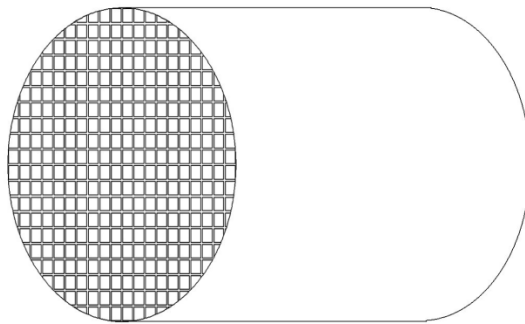
Fig. 1. Schematic of a typical monolith structure.

A catalytic monolith has a honeycomb structure with parallel channels (Fig. 1) and regular channel shapes (e.g., square, triangle, rectangle, or hexagon). The geometric parameters of the monolith include cell density, porosity, and dimensions of the monolith segment and thickness of the catalyst layer. The substrate material for the monolith can be ceramic or metallic and usually contains a thin layer of catalytic washcoat on the surface of the monolith channels.

Compared with conventionally packed pellets in a fixed-bed reactor, metallic monoliths have a larger void fraction, resulting in a pressure drop of up to two orders of magnitude lower, better heat transfer performance by using monolith substrate with a higher thermal conductivity, and a higher catalyst effectiveness factor (lower diffusional resistance due to thin catalyst layers on monolith surface) [12–13]. These advantages, especially the good heat transfer performance by heat conduction, make metallic monoliths very attractive for the strongly endothermic SMR process. This is despite the fact that improvements are still needed to lower the cost and develop proper methods for catalyst loading and design and assembly of the metallic monolith [14]. Early experimental [15] and modeling [16] studies compared the radial heat transfer between FeCralloy metal monoliths and pelletized catalysts in the absence of chemical reaction. A higher overall heat transfer coefficient, wall heat transfer coefficients, and lower effective radial thermal conductivity were observed in the modeling studies. The potential of metallic monoliths for use in a strong exothermic reaction was investigated by Groppi and Tronconi [17] using a pseudo-continuous heterogeneous 2D model. Good catalytic conversion and limited hot spot temperatures have been achieved through the proper design of monolithic catalyst parameters (e.g., volume fraction of washcoat and inert support, catalyst activity, and thermal conductivity of the support). With respect to the highly endothermic SMR process, Giroux et al. [10] reviewed the early studies on

monolith steam reformers and discussed the design and potential of a novel monolith reformer. FeCralloy metal monoliths have been used in experimental studies that investigated the catalyst preparation and characterization of supported nickel catalysts [18–20]. Comparative studies have also been performed between monolithic and other catalysts (powder [21, 22] and pellets [23]), where better performances have been observed for the monolithic catalyst. Recently, support materials with higher thermal conductivities than FeCralloy (16 W/m·K [23]), such as nickel (71 W/m·K [24]) [25–26] and SiC (350 W/m·K) [27] were investigated and good performance was achieved. The application of these highly conductive materials can further facilitate the development of novel monolithic steam reformers for small-scale hydrogen production.

Modeling methods such as computational fluid dynamics (CFD) can help further understand the heat transfer behaviors in monolithic catalysts with the aim of achieving better designs for application in various chemical processes. Chen et al. [28] reviewed the modeling methods for monolithic catalysts for gas phase reactions focusing on modeling in a single channel. With respect to multi-channel systems, Hayes et al. [29] performed 2-D CFD simulations for a quarter circular cross section of a monolith structure. The effective thermal conductivities under different conditions (channel shapes, with and without washcoat) have also been investigated. Schereth and Hinrichsen [30] compared a pseudocontinuous heterogeneous 2-D model with a 3-D CFD model (one-eighth of the monolith) for a monolith catalyst with a low channel number and exothermic reaction, and the 2-D model demonstrated results close to the 3-D CFD model under moderate reaction conditions. Cao et al. [31] investigated the effect of washcoat properties of 10% Ni catalyst for SMR in a plate microchannel reactor by using a two-dimensional CFD model. The SMR process is controlled by both internal mass transfer and reaction rate. An optimal washcoat thickness of around 75μm was found for washcoat layer. With respect to the design of a small-scale monolith steam methane reformer, however, there is still lack of relevant studies

regarding the selection and optimization of monolith configuration parameters, catalysts, and operating conditions.

The present study is aimed at providing quantitative analysis of the radial heat transfer performance for monolithic catalysts with an endothermic gas/solid reaction and different configuration parameters, for investigating the influence of the radial heat transfer on the potential and optimal design of a novel monolith steam methane reformer. Both pseudo-continuous and heterogeneous 2-D CFD simulations were performed, and the effective radial thermal conductivity and reforming capacity were investigated by considering the influence of the thermal conductivity of the monolith substrate, geometric parameters (cell density, porosity, and diameter), wall gap (between monolith and reactor wall), and radiation heat transfer.

2. CFD model and simulation approach

2.1 Geometry and the basic parameters

As shown in Fig. 2, one-eighth cross section of the monolith was investigated due to its symmetric structure. The "pizza bite" shape (Fig. 2(a) and (b)) was used for the simulations without chemical reaction (see section 3.1), whereas the shapes shown in Fig. 2(c)–(f) were used for the simulations with the endothermic gas/solid reaction. Fig. 2(b) and (d) show the pure solid without channels, which was used for calculating the effective thermal conductivity of the monolith structure and the parameter optimization by the pseudo-homogenous model (see section 3.5). The temperature and symmetry boundary conditions are presented in Fig. 2(b). Especially, the thickness of washcoat layer on the surface of the monolith channels was considered in Fig. 2(e) (see section 3.3). For monolith structures in Fig. 2(c) and Fig. 2(f), the thin-wall boundary condition in ANSYS FLUENT was set on the surface of the

monolith channels with a virtual washcoat thickness of $\delta'_{wash} = 0.3$ μm. The wall gap between the reactor wall and the monolith was considered in Fig. 2(f) (see section 3.4). Only the monolith structures with a porosity of 75.1% and cell density of 100 cpsc (cells per square centimeter) are illustrated. Monolith structures with other geometric parameters (porosity and cell density) were also investigated, but are not shown in Fig. 2.

In the square channels, a thermal conductivity of 0.1 W/m·K was set for the gas phase in all the CFD simulations, while much higher thermal conductivities (1–100 W/m·K) were assigned to the monolith substrates in the parameter studies. For a monolithic structure with square channels and a given radius, the number of the monolith channels is determined by the cell density Cd, and then the inner dimension of the square channel can be calculated by a given porosity ε and thickness of washcoat layer. In this study, the radius of the monolith $R = 9.9$ mm (i.e., a bench-scale tubular reactor), outer wall temperature $T_w = 973$ K (within the industrial SMR operating temperature range 723–1223 K [2]), porosity $\varepsilon = 75.1\%$, and cell density $Cd = 100$ cpsc (645 cells per square inch (cpsi)) were selected as the basic parameters for the following simulations if not stated otherwise. In industrial applications, a cell density of up to 1600 cpsi can be achieved with very thin walls in the monolith channels [32].
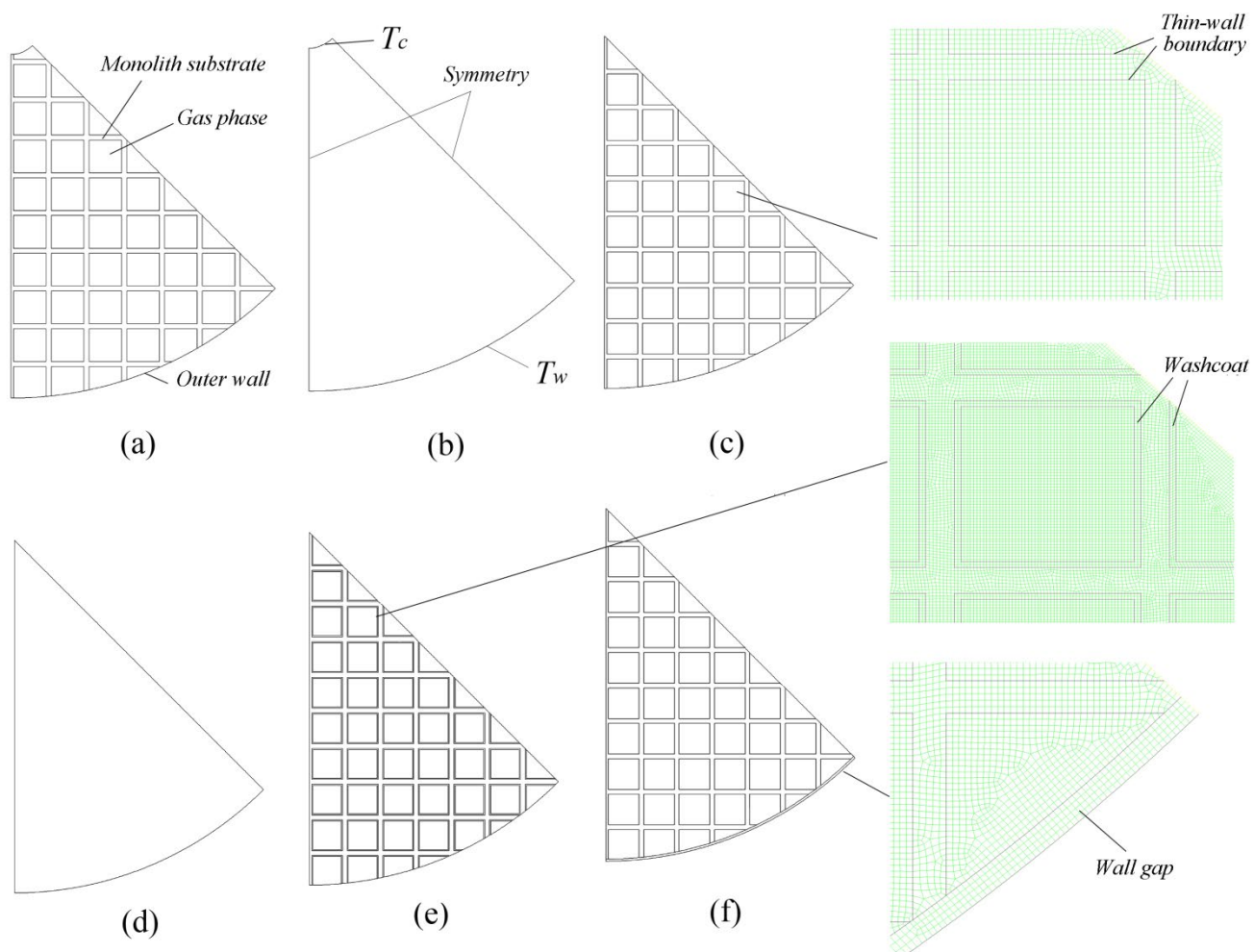
Fig. 2. Schematic of model geometries (porosity of the monolith substrates was 75.1%): (a). Monolith structure without chemical reaction; (b). Pure solid without chemical reaction; (c). Monolith structure with endothermic reactions; (d). Pure solid with endothermic reactions; (e). Monolith structure with washcoat and endothermic reactions; (f). Monolith structure with wall gap and endothermic reactions;

2.2 Mathematical model

2.2.1 Model assumptions

The 2-D model presented in this study focused on the radial heat transfer at the cross section of the monolith steam methane reformer with the following simplification and assumptions:

(1) A fully developed laminar flow was usually assumed for the gas phase due to the small diameter of the channels for a monolith structure [33], where the radial heat transfer (normal to the gas flow direction) for the gas phase in the channels of the monolith mainly occurs by molecular motion or heat conduction [34]. In the present 2-D model, the gas phase was set as static without consideration of the influence of the gas flow. In addition, the radial heat transfer are mainly through the highly conductive monolith substrate which has a much higher conductivity (e.g, 16 W/m·K) than that of the gas phase (e.g., 0.1 W/m·K).

(2) The thermal conductivity of the monolith substrate and the gas phase was assumed to be independent of temperature. At a high operating temperature (e.g., 973 K) for a monolith reformer, the changes of the conductivities for potential monolith substrate materials, i.e., stainless steel [35] and nickel [36], are within 5% when there is a temperature difference less than 100 K in the monolith structure. It should be noted that this temperature dependence should be considered if the conductivity of other selected materials which change strongly with temperature.

(3) In sections 3.2 and 3.4, the thickness of the catalytic washcoat was neglected and the thin-wall boundary condition was used (also see section 2.1).

(4) The axial heat and mass transfer and detailed SMR kinetics were not included in the 2-D model. Uniform catalyst layer or activity (at the same temperature) was assumed on the surface of the channels. The SMR reaction heat in the monolith channels was approximately evaluated from an industrial-scale reference value (see section 2.2.2). The height of the monolith structure in the 2-

D simulations was assumed to be 1 meter by ANSYS FLUENT for calculating the volumetric heat transfer rate.

2.2.2 Energy equation

The steady state energy equation for heat conduction is expressed by:
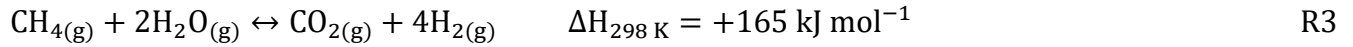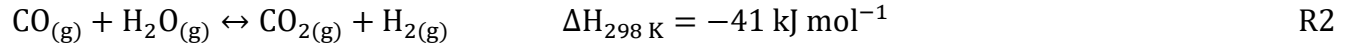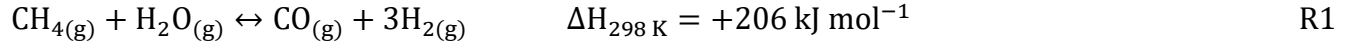
$$\nabla \cdot (\lambda \nabla T) + S_R = 0 \tag{1}$$

$$S_R = -Q_{wash} \tag{2}$$

$$Q_{wash} = Q_{mono,avg} \times \frac{V_{mono}}{\delta_{wash} S_{ch}} \tag{3}$$

where S_R is the volumetric heat source (W/m^3), Q_{wash} is the reaction heat based on the volume of the catalytic washcoat, $Q_{mono,avg}$ is the average reaction heat for the bulk monolithic bed, and V_{mono} is the corresponding monolith volume. S_{ch} is the surface area of the monolith channels. In this study, a reference value of $Q_{wash,ref}= 3.6 \times 10^7$ W/m^3 was assumed as the value of Q_{wash} at 973 K, which was evaluated by equation (3) and according to previously reported values (average heat flux of tube wall 90 kW/m^2 [37], catalyst effectiveness factor of 0.1 [38], porosity of 0.5, and tube diameter of 200 mm [2]) for industrial-scale packed bed SMR tubular reactors. It should be noted that actual heat consumed by SMR also depends on the axial position, i.e., being higher at the reactor inlet. In the present study, uniform heat flux along the tube wall was assumed for the evaluation of $Q_{wash,ref}$. A thickness of $\delta_{wash} = 30$ μm was assumed for the washcoat layer in the monolith structures. Note that for the CFD models in sections 3.2 and 3.4, the thin-wall boundary condition was used and a virtual washcoat thickness of $\delta'_{wash} = 0.3$ μm was set $Q_{wash,ref}$ was adjusted with $\delta_{wash} / \delta'_{wash}$ and equal to 3.6×10^9 W/m^3.

The conventional endothermic SMR process for hydrogen production includes the following reactions [2]:

$$CH_{4(g)} + H_2O_{(g)} \leftrightarrow CO_{(g)} + 3H_{2(g)} \qquad \Delta H_{298\,K} = +206 \text{ kJ mol}^{-1} \qquad \text{R1}$$

$$CO_{(g)} + H_2O_{(g)} \leftrightarrow CO_{2(g)} + H_{2(g)} \qquad \Delta H_{298\,K} = -41 \text{ kJ mol}^{-1} \qquad \text{R2}$$

$$CH_{4(g)} + 2H_2O_{(g)} \leftrightarrow CO_{2(g)} + 4H_{2(g)} \qquad \Delta H_{298\,K} = +165 \text{ kJ mol}^{-1} \qquad \text{R3}$$

where part of the CO in the reforming process (R1) is converted to CO_2 by the exothermic water gas shift reaction (R2). Under the investigated conditions (i.e., temperature, pressure and steam-to-carbon ratio of 3) in this study, the thermodynamic equilibrium composition and the total enthalpy change $\Delta H_{total,T}$ for the SMR reactions were evaluated by the commercial software Aspen Plus V9. The reaction rate of the key component CH_4 (R_{wash}) in the catalytic washcoat can be calculated by:

$$R_{wash} = \frac{Q_{wash}}{\Delta H_{total,T}} \qquad (4)$$

In the monolith channel, the internal mass transfer resistance in the thin washcoat layer (30μm) is neglected. At the high operating temperature (e.g., 973 K), the external mass transfer rate of the key component CH_4 from the bulk gas phase to the channel surface has been evaluated which is in the range of 10^{-1}–10 mole/m^2·s, while the evaluated reaction rate of CH_4 according to equation (4) and the reference reaction heat $Q_{wash,ref}$ is around 0.5×10^{-2} mole/m^2·s. Therefore the external mass transfer resistance can be also neglected. Assumed that the reaction rate is simply first order in CH_4, R_{wash} can be expressed by [39]:

$$R_{wash} = k_{CH4,T} P_{CH4} \qquad (5)$$

where P_{CH4} is the partial pressure of CH_4, $k_{CH4,T}$ is the reaction constant at certain temperature. According to equations (4)–(5) and the Arrhenius equation, the temperature dependence of R_{wash} can be given by:

$$R_{wash} = k_{CH4,T_{ref}} exp\left[-\frac{E}{R}(\frac{1}{T} - \frac{1}{T_{ref}})\right] = \frac{Q_{wash,ref}}{\Delta H_{total,T_{ref}}} exp\left[-\frac{E}{R}(\frac{1}{T} - \frac{1}{T_{ref}})\right] \qquad (6)$$

where R is gas constant, T_{ref} is the reference temperature (T_{ref} = 973 K), E is the activation energy, in this study E = 96100 J/mole was selected [39]. Considering equations (4) and (6), the temperature dependence of the volumetric heat source, S_R, can be derived:

$$S_R = -Q_{wash} = R_{wash}\Delta H_{total,T} = \frac{\Delta H_{total,T}Q_{wash,ref}}{\Delta H_{total,T_{ref}}} exp\left[-\frac{E}{R}(\frac{1}{T} - \frac{1}{T_{ref}})\right] \qquad (7)$$

Similarly, for the solid structure in Fig. 2(d), S_R can be expressed by:

$$S_R = -Q_{mono,avg} = \frac{\delta_{wash}S_{ch}\Delta H_{total,T}Q_{wash,ref}}{V_{mono}\Delta H_{total,T_{ref}}} exp\left[-\frac{E}{R}(\frac{1}{T} - \frac{1}{T_{ref}})\right] \qquad (8)$$

2.2.3 Radiation Model

Many radiation studies on monolithic structures can be found in literature [40–45], e.g., for catalytic automobile radiation in the monolithic channels (from wall to wall) or near the outer wall of the monolith may influence the heat transfer behavior in a monolithic reactor. Due to the high operating temperatures of the SMR process (e.g., up to 1173 K), the influence of radiation on the monolithic reformer was also considered in the present CFD model and investigated in sections 3.1 and 3.4. The discrete ordinates (DO) radiation model and the surface-to-surface (S2S) radiation model were selected in the present CFD model. The DO model covers the entire range of optical thickness and has a moderate computational cost with the following radiative transfer equation (RTE) [46]:

$$\nabla \cdot (I(\vec{r}, \vec{s})\vec{s}) + aI(\vec{r}, \vec{s}) = an^2 \frac{\sigma T^4}{\pi} \tag{9}$$

where r and s are the direction and position vectors, respectively, a is the adsorption coefficient, I is the radiation intensity, n is the refractive index, and σ is the Stefan-Boltzmann constant (5.669×10^{-8} W/m^2·K^4). Radiation scattering was neglected in these computational procedures.

The S2S model only includes the radiation between surfaces with a lower computational cost, and can be expressed by [46]:

$$q_{out,k} = \varepsilon_k \sigma T_k^4 + \rho_k \sum_{j=1}^{N} F_{kj} q_{out,j} \tag{10}$$

where $q_{out,k}$ and $q_{out,j}$ are the energy fluxes leaving surface k and j, ε_k is the emissivity, ρ_k is the refractivity, F_{kj} is the view factor (the fraction of the energy flux leaving surface j which is incident on surface k).

2.3 Solution method

Steady state simulations were conducted using the commercial finite-volume-based solver ANSYS FLUENT 18.0 in the parameter optimization studies with double-precision. The energy and radiation equations were solved using a second-order upwind discretization scheme. Residual levels of 10^{-10}, 10^{-13} and 10^{-5} were used for the energy and radiation equations in the DO and S2S radiation model, respectively. Three angular discretizations of 4×4, 4×8, and 4×16 were set for the DO radiation model, and the change of the total heat transfer rate through the monolith Q_m was not obvious (within 0.1%), so the angular discretization of 4×4 was chosen. A pixelation of 3 was also set for the DO model [46]. The absorption coefficients for the gas and solid phases were 0 and 0.7, respectively, while the refractive

index was 1 for the gas phase and 0 for the monolith support. The ray tracing method was used for computing the view factors in the S2S radiation model. The mesh independence was checked (with mesh sizes of 17–67 µm) for the geometry in Fig. 2(a), and a mesh size of 25 µm with 59124 quadrilateral elements was applied (part of the mesh was shown in Fig. 2). The change of the total heat transfer rate through the monolith Q_m was calculated by using a smaller mesh size (17 µm, 137365 elements) and was within 0.2% of the original. Similar mesh sizes (15–33 µm) were applied for other monolith structures in Fig. 2 and also monolith structures with different porosities and cell densities in this study.

2.4 Effective thermal conductivity

The effective thermal conductivity with regards to the overall heat resistance in a monolithic structure is usually calculated by a pseudo-continuous model. In the radial direction, the effective thermal conductivity, $k_{r,eff}$, can be estimated by the series [47], parallel [29], and symmetric models [48]. All the models are based on electrical analogy between thermal and electrical resistance for a square monolith cell. In the absence of washcoat, $k_{r,eff}$ can be calculated by the parallel model [29] with:

$$k_{r,eff} = k_s (1 - \sqrt{\varepsilon} + \frac{\sqrt{\varepsilon}}{1 - \sqrt{\varepsilon} + \frac{k_s}{k_f}\sqrt{\varepsilon}}) \tag{11}$$

and the symmetric model [48] with:

$$k_{r,eff} = k_s \frac{\frac{k_f^2}{k_s^2}\frac{1-\varepsilon}{1+\varepsilon} + \frac{k_f}{k_s}\frac{3\varepsilon^2 + 2\varepsilon + 3}{(1+\varepsilon)^2} + 2\frac{1-\varepsilon}{1+\varepsilon}}{\frac{k_f^2}{k_s^2}(\frac{1-\varepsilon}{1+\varepsilon})^2 + 3\frac{k_f}{k_s}\frac{1-\varepsilon}{1+\varepsilon} + 2} \tag{12}$$

where k_s and k_f are the thermal conductivity of the monolith substrate and gas phase respectively.

18

Hayes et al. [29] studied the influence of the catalyst layer on a non-reactive monolith and reported a slight increase in the G factor compared with the blank monolith. In the present of washcoat, the the effective thermal conductivity, $k_{r,eff}$, can be calculated by the parallel model [29] with:

$$k_{r,eff} = k_s(1 - \sqrt{\varphi + \xi} + \frac{\sqrt{\varphi + \xi} - \sqrt{\varphi}}{1 - \sqrt{\varphi + \xi} + \frac{k_s}{k_w}\sqrt{\varphi + \xi}} + \frac{\sqrt{\varphi}}{1 - \sqrt{\varphi + \xi} + \frac{k_s}{k_w}(\sqrt{\varphi + \xi} - \sqrt{\varphi}) + \frac{k_s}{k_f}\sqrt{\varphi}})$$

(13)

and the symmetric model [48] with:

$$k_{r,eff} = k_s \frac{\frac{k^2}{k_s^2}\frac{1 - (\varphi + \xi)}{1 + (\varphi + \xi)} + \frac{k}{k_s}\frac{3(\varphi + \xi)^2 + 2(\varphi + \xi) + 3}{(1 + (\varphi + \xi))^2} + 2\frac{1 - (\varphi + \xi)}{1 + (\varphi + \xi)}}{\frac{k^2}{k_s^2}(\frac{1 - (\varphi + \xi)}{1 + (\varphi + \xi)})^2 + 3\frac{k}{k_s}\frac{1 - (\varphi + \xi)}{1 + (\varphi + \xi)} + 2}$$

(14)

$$k = k_w \frac{\frac{k_f^2}{k_w^2}\frac{1 - \varphi}{1 + \varphi} + \frac{k_f}{k_w}\frac{3\varphi^2 + 2\varphi + 3}{(1 + \varphi)^2} + 2\frac{1 - \varphi}{1 + \varphi}}{\frac{k_f^2}{k_w^2}(\frac{1 - \varphi}{1 + \varphi})^2 + 3\frac{k_f}{k_w}\frac{1 - \varphi}{1 + \varphi} + 2}$$

(15)

where φ is the volume fraction of the gas phase, ξ is the volume fraction of the washcoat and k_w is the thermal conductivity of the washcoat.

3. Results and discussion

3.1 Effective thermal conductivity for non-reactive monolith structure

2-D CFD modeling for a quarter section of a circular monolith has been demonstrated to be comparable with the parallel model in [29], where the $k_{r,eff}$ and a non-dimensional G factor for a row of four square channels were defined by the following equations:

$$k_{r,eff} = q \times \left(\frac{\Delta T}{W}\right)^{-1} \tag{16}$$
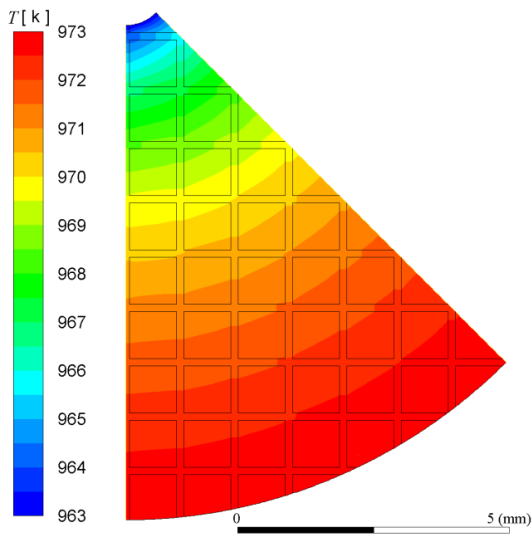
$$G = \frac{k_{r,eff}}{k_s} \tag{17}$$

where q is heat flux, W is the overall cell dimension. In the present study, this G factor was used to evaluate the effective thermal conductivity of monolith structures, according to equations (16) and (17), the G factor can be calculated by:

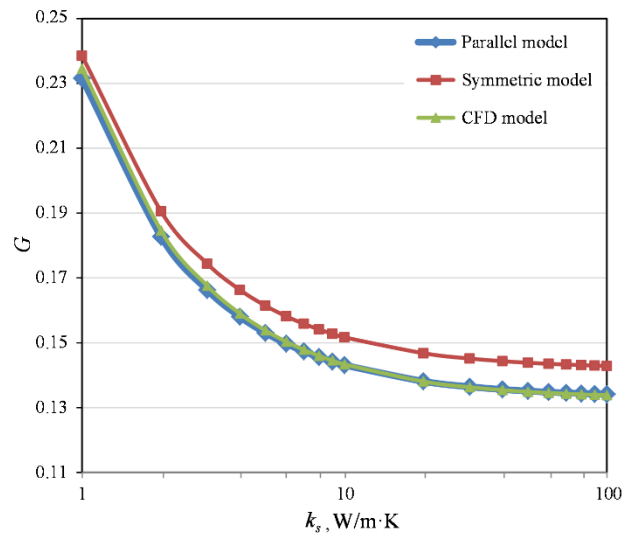$$G = \frac{Q_m}{Q_s} \times \frac{\Delta T_s}{\Delta T_m} \tag{18}$$

where ΔT_m and ΔT_s are the temperature differences between the outer wall and the center ($T_w - T_c$) of the structures in Fig.2(a) and Fig. 2(b) respectively, and T_c and T_w were set to 963 and 973 K, respectively. Q_m and Q_s are the total heat (W) transfer rate through the monolith structure and pure solid (Fig. 2(a) and (b)) respectively which were calculated from the heat transfer rate at the outer wall. The endothermic SMR reaction heat was not included in this section. The effective thermal conductivities and G factor provided by the CFD simulations (according to equation (18)) were compared with the values predicted by the parallel model and symmetric model where the $k_{r,eff}$ value was calculated by equations (11) and (12) for the two models.

The temperature distribution of the monolith structure in Fig. 2(a) was shown in Fig. 3(a). The temperature gradient was approximately along the radial direction from the outer wall to the center, and
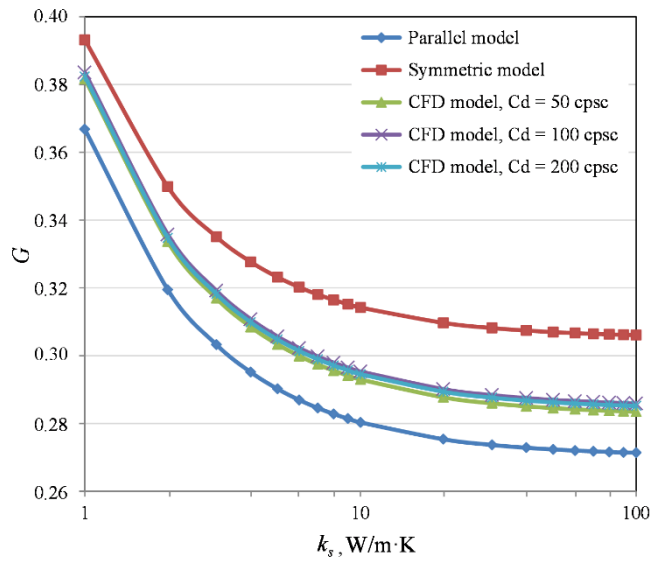
slightly influenced by the local monolith structures. Fig. 3(b) shows the variation of the G factor with the thermal conductivity of the monolith substrate ($\varepsilon = 75.1\%$, Fig. 2(a)). A steep change in G factor was observed near the low k_s area, while the change is much smaller when the k_s is high ($k_s > 30$ W/m·K). Good agreement between the numerical solution and the prediction by the parallel model was noticed, which is consistent with the results reported in other works [29]. The symmetric model provided good prediction for the G factor of a single square channel over the whole range of porosity in [48]. In this study for a multi-channel monolith structure, compared with the numerical simulations, an overestimation of the G factor (<7%) was observed for the symmetric model. The G factor for the monolith with a lower porosity ($\varepsilon = 53.2\%$) was also investigated, as shown in Fig. 3(c). A similar level of overestimation (<7%) was obtained with the symmetric model, while an underestimation (<5%) was obtained with the parallel model. This is in line with previous studies for a single square channel [48] where the prediction accuracy of the parallel model decreased significantly under low ε conditions. Nevertheless, compared with the numerical simulations, both the two pseudo-continuous models provide acceptable prediction accuracies with respect to the G factor (effective thermal conductivity) for a multi-channel monolith structure with the investigated porosities. The influence of cell density on the G factor was also investigated as shown in Fig. 3(c), which is found not to be significant in the range of 50–200 cpsc.

Fig. 3 (a) Temperature distribution of the monolith structure (ε =75.1%, Cd = 100 cpsc); Variation of the G factor with thermal conductivity of the monolith substrate: (b) ε =75.1%, Cd = 100 cpsc; (c) ε = 53.2%, Cd = 50-200 cpsc.

The radiation heat transfer in the monolith channels was then considered based on the above simulations. The DO model and S2S model were taken into account in the CFD model. The influence of the radiation heat transfer can be expressed by the following enhancement factor:

$$f = \frac{G_{rad} - G}{G} \times 100\% \tag{19}$$

where G_{rad} is the G factor with radiation heat transfer added in the model. Fig. 4(a) shows the enhancement factor f with different thermal conductivities of the monolith substrate and outer wall temperatures ($T_w = 973$–1173 K). The trend is similar to that seen in Fig. 3. Because the radiation heat transfer rate is determined by the temperature of the monolith substrate according to the Kirchhoff's law, when T_w and ΔT were fixed, the change of the radiation heat transfer rate with the variation of the conductivity, k_s, is insignificant. In contrast, it is obvious that the conductive heat transfer rate decreases with the decrease of k_s. Consequently, the proportion of the radiation heat transfer increased with a decrease of k_s. Higher radiation heat transfer rates were obtained by increasing the outer wall temperature, T_w, with a 33–37% increase of f from 973 to 1073 K and 29–30% increase of f from 1073 to 1173 K. The influence of the ΔT value on the radiation heat transfer was not significant. It is clear that by using highly conductive monolith substrates such as nickel ($k_s = 71$ W/m·K at 973 K) the influence of the radiation heat transfer is negligible ($f < 1.5\%$) under the investigated conditions in Fig. 4(a). When using FeCralloy ($k_s = 16$ W/m·K) as monolith substrate, more attention should be paid to the influence of radiative heat transfer, especially at high temperatures (e.g., $T_w = 1173$ K). With respect to the radiation models, both models generated close results under the investigated conditions with differences less than 1% (for the S2S model, only the results with $T_w = 973$ K and $\Delta T = 10$ are shown in the figure). Therefore, the DO model was used for the following simulations related to radiation heat transfer if not stated otherwise.

The radiation heat flux of the channel walls was illustrated in Fig. 4(b) under the condition of k_s = 16 W/m·K and T_w = 1173 K. The radiation heat transferred from the lower part to the upper part of the channel in the figure (heat flux from the wall surface is positive). The radiation heat flux for the walls near the center are more obvious, which indicates a higher temperature change in this area. In addition, the influence of monolith porosity (53.1–88.1%) and cell density (50–200 cpsc) on the f value (with T_w = 973 K and ΔT =10) are shown in Fig. 4(b). The simulation results provided by the two radiation models are also very close (only the results with ε = 88.1% and Cd =100 cpsc are shown for the S2S model in the figure). An increase of cell density resulted in lower f values. This can be attributed to more channel walls in the monolith structure which raised the number of times of the radiation absorption (with an absorption coefficient equal to 0.7) and emissivity on the wall surface and lower the efficiency of radiation heat transfer. In contrast, the f value significantly increased with the increase of the monolith porosity, ε. Specifically, the f value increased by a factor of two to three when changing the monolith porosity from 64.2% to 88.1%, and the f value achieved 7.3% by using FeCralloy monolith. Under the conditions with higher outer wall temperature and lower cell density, the f value can be higher than this value. However, the influence of the radiation heat transfer could be low if a highly conductive monolith substrate is used (e.g. k_s = 71 W/m·K). The influence of the radiation heat transfer was further discussed in the following section 3.3.
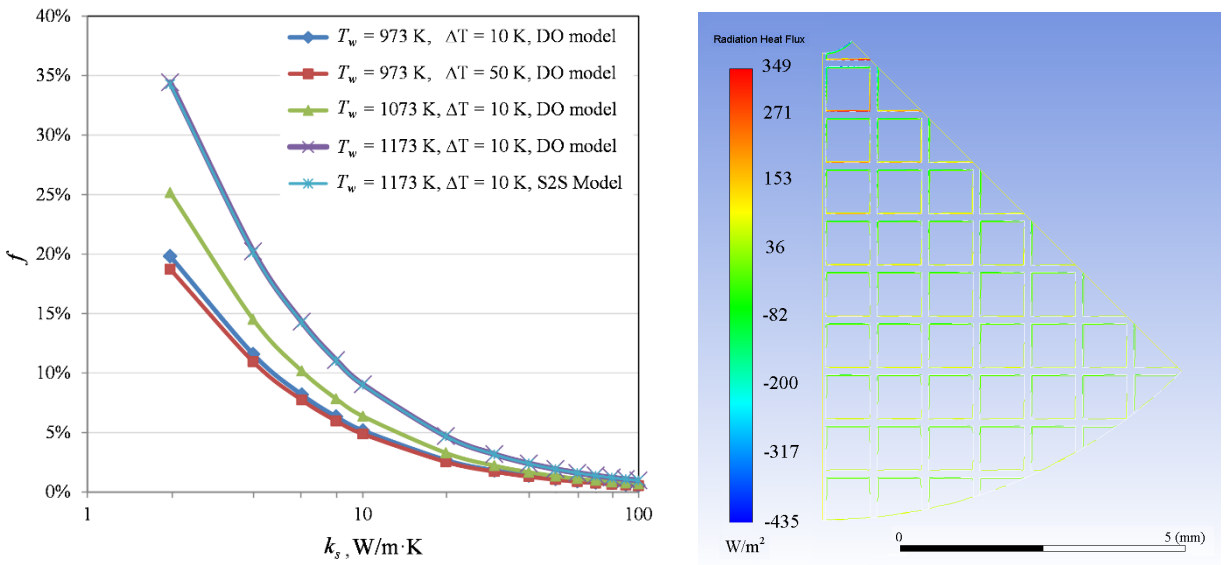
(a)

(b)
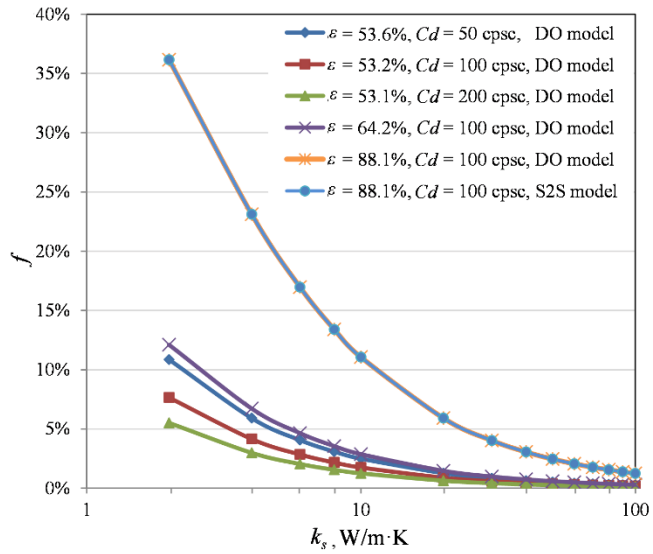
(c)

Fig. 4 (a) Variation of enhancement factor f with thermal conductivity of the monolith substrate with different temperature arrangements, $\varepsilon = 75.1\%$ and $Cd = 100$ cpsc; (b) radiation heat flux of the channel walls, $k_s = 16$ W/m·K, $T_w = 1173$ K; (c) variation of the factor f with k_s, porosities and cell densities of monolith.

3.2 Influence of the SMR reactions

Considering the endothermic SMR reactions, a large amount of heat transfer from the outer wall occurs and is consumed gradually when travelling through the monolith reformer in the radial direction, which is significantly different from the conditions without reactions (section 3.1). The SMR reaction heat calculated by equation (7) was added to the wall surface of the monolith channels in Fig. 2(c) ($\varepsilon = 75.1\%$) by a user defined function where $Q_{wash, ref} = 3.6 \times 10^6$ kW/m^3, and thin-wall boundary condition was used Monoliths with porosities of 45%, 53.2%, 64.2%, and 88,1% were also investigated (not shown in Fig. 2). The G factor was calculated by equation (18) as mentioned in section 3.1, where ΔT_m and ΔT_s are the temperature differences between the outer wall and the center (T_w - T_c) of the structures in Fig.2(c) and Fig. 2(d), respectively. T_w was set to 973 K, and T_c was provided by the simulations which is the temperature close to the center of the monolith (usually the minimum temperature in the monolith). Q_m and Q_s were calculated from the heat transfer rate at the outer wall of the structures in Fig. 2(c) and Fig. 2(d), With respect to the solid structure in Fig. 2(d), The reaction heat was set on the whole structure, and the $Q_{wash,ref}$ value (for the calculation of S_R) was adjusted to achieve an equal value of Q_m and Q_s (equal heat consumed in the two structures). The G factor was then calculated by the ratio of ΔT_s and ΔT_m.
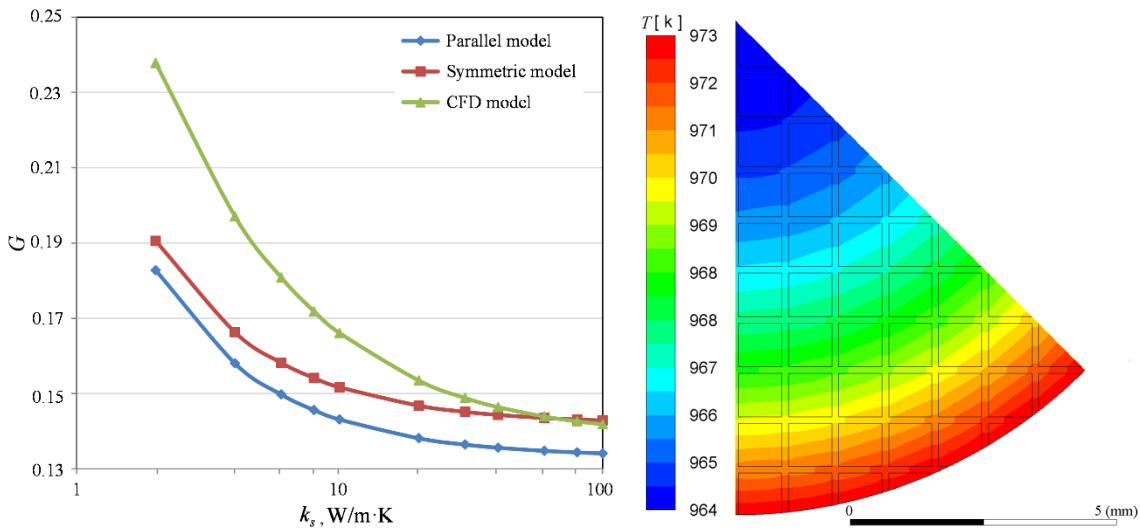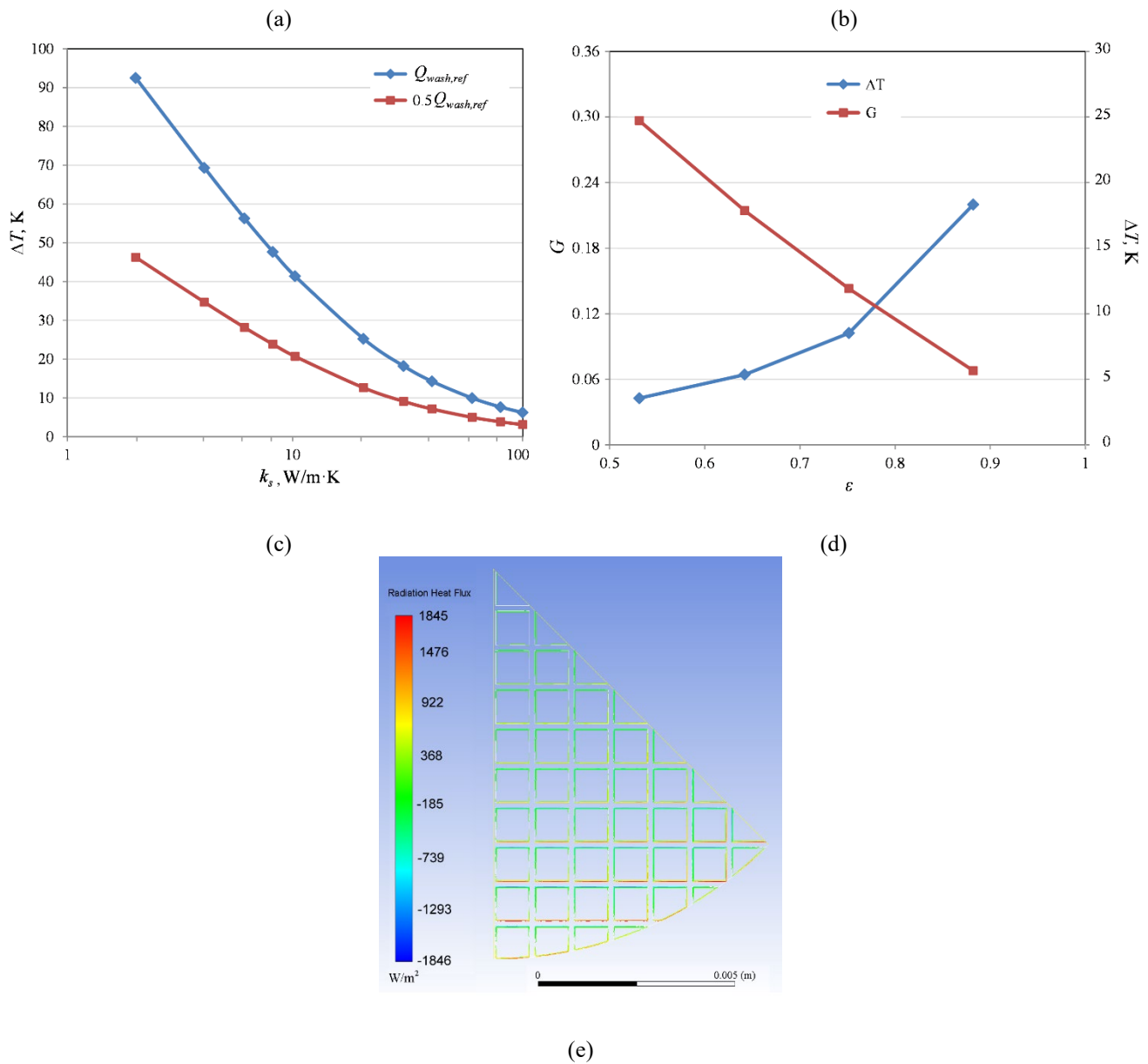
Fig. 5 (a) Variation of the *G* factor with thermal conductivity of the monolith substrate for the monolith reformer; (b) Temperature distribution of the monolith reformer (k_s = 71 W/m·K); (c) Variation of ΔT with the thermal conductivity of the monolith substrate; (d) influence of the monolith porosity on the *G* factor and ΔT (k_s = 71 W/m·K); (e) radiation heat flux of the channel walls, k_s = 16 W/m·K, T_w = 973 K;

Fig. 5(a) shows the variation in the *G* factor with the thermal conductivity of the monolith substrate for the monolith reformer. Compared with the CFD simulations without reactions in Fig. 3(a), the *G* factor

is higher, and in the low k_s area the G factor increased faster with the decrease of the k_s values. This difference is attributed to the change of the distribution of the heat flux in the monolith. According to the geometry shown in Fig. 2(c), there are more channels near the outer wall where more heat is consumed by the endothermic SMR reactions in the radial direction. In addition, along the radial direction of the circular monolith geometry (from outer wall to center), the heat transfer resistance and reaction rate increased and decreased, respectively, due to the decrease of cross sectional area and temperature. Consequently, more heat load is distributed to the areas with larger cross sectional area and lower heat resistance (close to the outer wall), which results in a lower overall heat resistance and higher effective thermal conductivity compared with the conditions without reactions (section 3.1). Compared with the CFD simulations, the results from both the parallel and symmetric models are underestimated. In moderate and high k_s area (k_s >10 W/m·K), the two models give acceptable accuracy (<10% error for the symmetric model and <15% error for the parallel model) for the prediction of the G factor. With respect to relevant experimental investigation on the radial heat transfer of a monolith reformer, there is few study reported. A Fecralloy (k_s = 16 W/m·K, ε = 45%) monolithic reformer was investigated in [23]. The average effective thermal conductivity in the radial direction of the monolithic reformer can be evaluated from the experimental data, and the calculated G factors are around 0.11–0.23. In the present study, predictions under the same conditions (k_s = 16 W/m·K, ε = 45%, Cd =102 cpsc) were conducted, and the G factors are 0.34, 0.38 and 0.37 by the parallel model, symmetric model and CFD simulation respectively which are higher than that evaluated from the experimental data. Because other heat resistance, especially the gap between the monolithic bed and the reactor tube was also included in the experimental study of the monolith reformer which could obviously decrease the effective thermal conductivity and the G factor (see section 3.4). Fig. 5(b) illustrates the temperature distribution of the monolith reformer with k_s = 71 W/m·K. The temperature decreased from the outer wall to the center of

the monolith reformer due to the endothermic reactions. Compared to the temperature profile in Fig. 3(a), steeper temperature drop near the outer wall and flat temperature profile close to the center point were found, which indicates a larger heat load near the outer wall as mentioned above. Fig. 5(c) gives a further demonstration of the variation of ΔT with the thermal conductivity of the monolith substrate under two $Q_{wash,ref}$ values. The trend of ΔT indicates that the use of a highly conductive monolith substrate such as nickel can achieve nearly isothermal conditions, whereas using materials with low thermal conductivity (especially in the low k_s area) will significantly increase ΔT. The use of FeCralloy results in a moderate ΔT and better overall heat transfer performance in the radial direction than the pelletized packed bed [16, 23]; however, using a highly conductive monolith substrate increases the possibility of further intensification of a SMR reformer, e.g., a design with larger tube diameter. Fig. 5(d) shows the influence of monolith porosity on the G factor and ΔT. With an increase in monolith porosity from 53.2% to 88.1%, the G factor decreased significantly from 0.297 to 0.068 and the ΔT value increased from 3.6 to 21.6 K. High porosity is one of the advantages of the metallic monolith, which results in lower material costs and pressure drop; however, lower effective thermal conductivity is an unfortunate side effect of the porosity. Hence, an overall consideration is needed for the selection of monolith porosity as well as for the selection of other parameters such as effective thermal conductivity, thickness of washcoat, diameter of monolith, cell density, and cost, which are further discussed below. The radiation heat flux of the channel walls was also illustrated in Fig. 5(e). The radiation heat transfer is more obvious near the outer wall, which is different from the trend in Fig. 4(b) and also indicates a larger temperature change in this area under the condition with the SMR reactions. The values of the enhancement factor f by radiation heat transfer were lower than those under the condition without the SMR reactions. To evaluate the importance of the radiation heat transfer under different conditions, the following expression has been developed:

$$f = \frac{4\sigma\varepsilon^2 dT_w^3}{k_{r,eff}} \tag{20}$$

where σ is the Stefan-Boltzmann constant (5.670×10^{-8} W/m$^2\cdot$K^4), ε is the emissivitiy for the surfaces in the monolith channels, d is the side length of the channel, T_w is the outer wall temperature of the monolith. More explanation of equation (20) can be found in Appendix A.

3.3 Influence of the catalyst layer

In the present study, the influence of the catalyst layer on the G factor was investigated for a reactive monolith in the CFD model. A thin catalyst layer of 30 μm was added on the monolithic channels as shown in Fig. 2(e). $Q_{wash,\ ref}$ (3.6×10^7 W/m^3), $0.5Q_{wash,\ ref}$ (1.8×10^7 W/m^3) and $2Q_{wash,\ ref}$ (7.2×10^7 W/m^3) were used for the calculation of the volumetric reaction heat (equation (7)) in the washcoat layer. The G factor was calculated as described in section 3.2. Thermal conductivity of 1 W/m$\cdot$K was set for the catalyst layer. The influence of washcoat layer on the G factor can be expressed by

$$f_{wash} = \frac{G_{wash} - G}{G} \times 100\% \tag{21}$$

where G_{wash} is the G factor with the consideration of the washcoat layer. Fig. 6(a) shows the G factors at different $Q_{wash,\ ref}$ and k_s values where the $k_{r,eff}$ values for the parallel and symmetric model were calculated by equations (13) – (15). The symmetric model is in good agreement with the CFD model with a deviation of less than 10% for most k_s values ($k_s > 4$ W/m$\cdot$K) and the three $Q_{wash,\ ref}$ values, which is better than results for the condition without consideration of washcoat layer in Fig. 5(a). The results provided by the parallel model were underestimated. The G factor increase with the increase of $Q_{wash,\ ref}$ value, which indicates the change of temperature distribution in the monolith structure by the endothermic SMR reactions mentioned in section 3.2. Fig. 6(b) shows the increment of the G factor (f_{wash})

compared to the results in Fig. 5(a) for a zero thickness of the washcoat. The increment enlarged with a decrease of the k_s value, and is less than 5% when $k_s > 8$ W/m·K. It is clear that by using a highly conductive monolith substrate, the thermal influence of the washcoat on the G factor is not significant in this study, then the less complex CFD model without considering the washcoat layer (see Fig. 2(c)) can be used for the evaluation of the G factor. However, washcoat layers with other thicknesses and materials and other factors such as catalyst activity, mass transfer in the washcoat layer, and pressure drop in the channel should still be considered for the design of the washcoat.
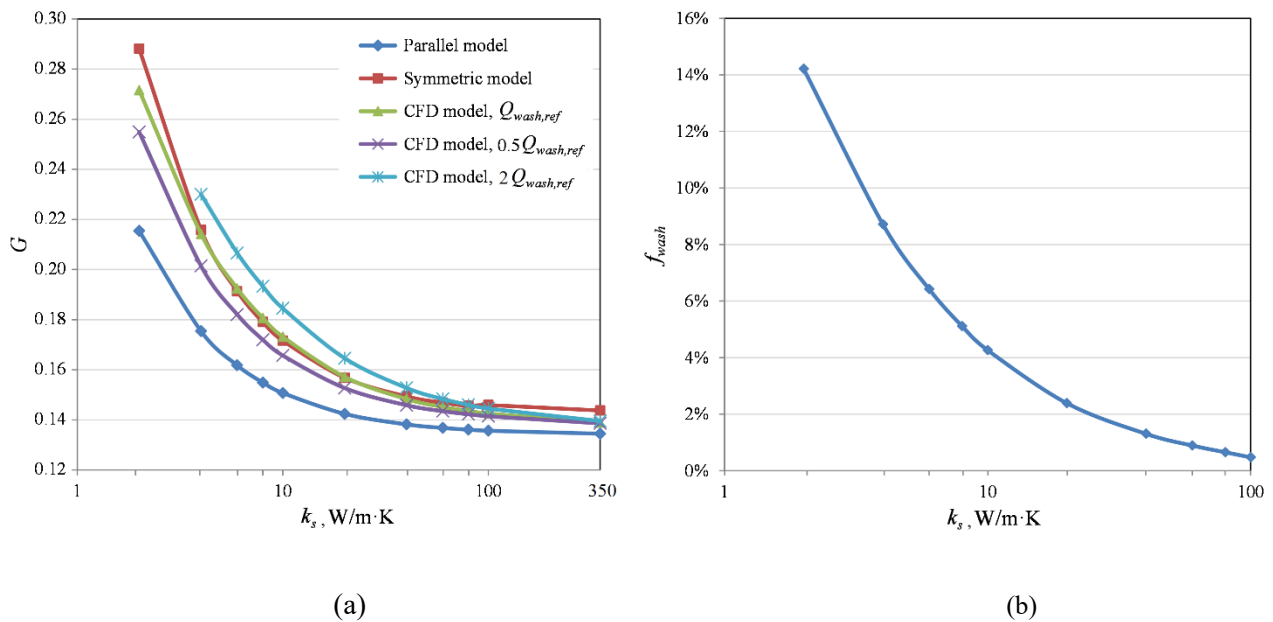

(a)   (b)

Fig. 6 (a) Variation of the G factor with thermal conductivity of the monolith substrate with washcoat layer; (b) Increment of the G factor compared to the condition with zero thickness of washcoat.

3.4 Influence of the wall gap

It is clear that a monolithic catalyst can provide a higher wall heat transfer coefficient than a pelletized catalyst due to a larger contact area between the monolith and the reactor wall. However, a "gap" between the monolith skin and the reactor wall is usually unavoidable, which could be the major contributor to

the thermal resistance for radial heat transfer in monolith reactors [49]. The wall gap problem could be improved by using a thermal expanding mat (3M Interam) [10] between the monolith skin and the reactor wall, however, the mat usually has a low conductivity. In the present study, the influence of gap resistance on the effective thermal conductivity was investigated under the condition with the endothermic SMR reactions. A thin gap was added outside the monolith geometry as shown in Fig. 2(f), with gap thicknesses of 0.05, 0.1, and 0.2 mm. Thermal conductivities in the range 0.1–0.3 W/m·K (typical range under the temperature and composition conditions for SMR) were chosen for the gas phase in the monolith channels and for the gap outside the monolith. The G factor was calculated as described in section 3.2. The ratio of the G factors with and without a gap was calculated to determine the influence of the gap, which can be expressed by G_{gap}/G (or $k_{r,eff,gap}/k_{r,eff}$), where G_{gap} and $k_{r,eff,gap}$ are the G factor and effective thermal conductivity with the consideration of the wall gap.

Fig. 7(a) shows the values of G_{gap}/G with different gas and solid phase conductivities and gap thicknesses. The influence of the gap resistance is more significant for highly conductive monolith support materials. For example, with k_s = 71 W/m·K and k_f = 0.3 W/m·K, a thickness as small as 0.05 mm results in more than a 40% decrease of $k_{r,eff}$. For the larger gap thickness (0.2 mm) and lower gas-phase conductivity (k_f = 0.1 W/m·K), the decrease of $k_{r,eff}$ was more than 80%. The heat transfer coefficient of the gap can be expressed by $h_{gap} = \delta/k_f$ [50], and it is clear that the gap resistance decreased with an increase of the gas-phase conductivity. With respect to a SMR process, the gas-phase temperature and composition differ along the axial direction of a reformer, which could result in different k_f values and gap resistances (e.g., k_f is 0.12 W/m·K for the feed gas at 973 K and a steam-to-carbon ratio of 3, while k_f is 0.21 W/m·K for the gas mixture with 80% conversion of the methane gas). In addition, the difference of the thermal expansion coefficients for the monolith substrate and the reactor wall should also be considered, as it could enlarge or reduce the gap thickness when temperatures are raised to the high operating temperatures

(e.g., 973 K). Different local temperatures of a reformer (e.g., different temperatures along the axial direction) could also result in different rates of expansion.
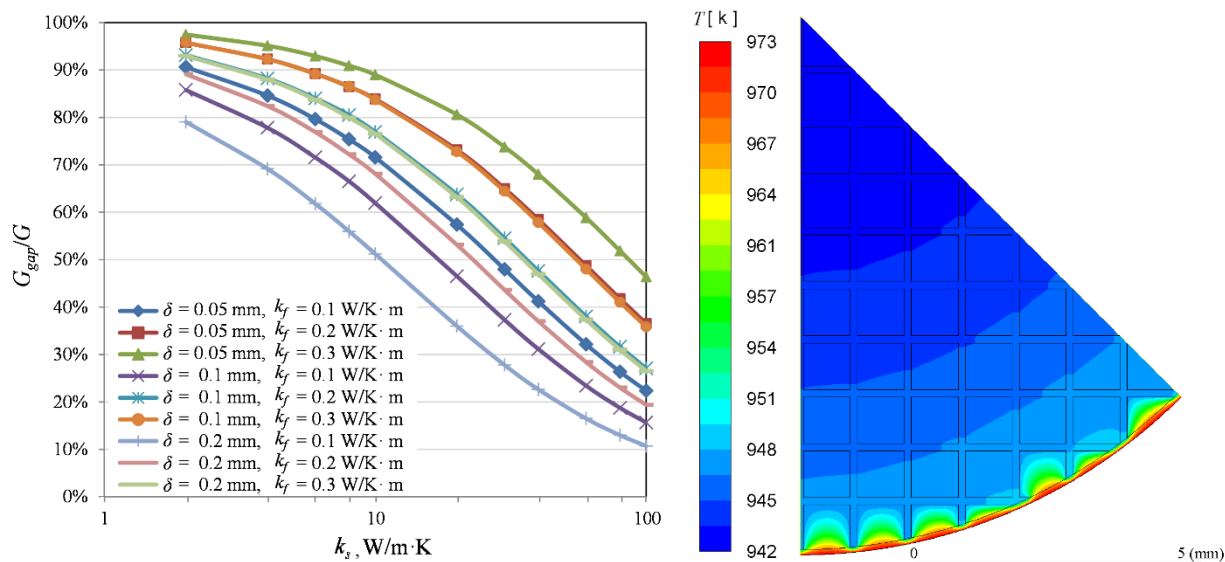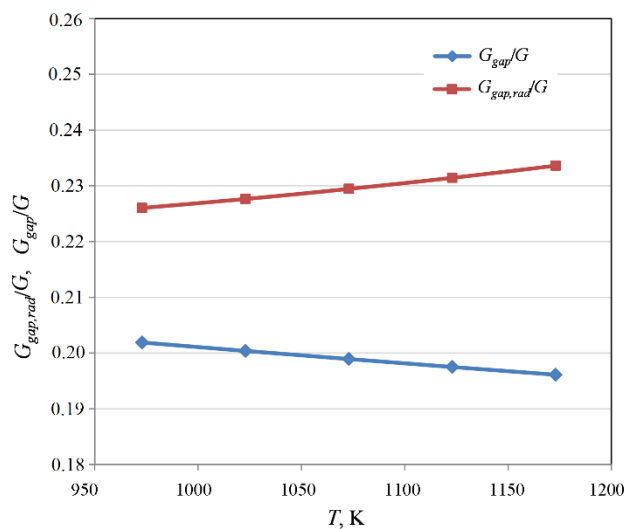

(a)

(b)
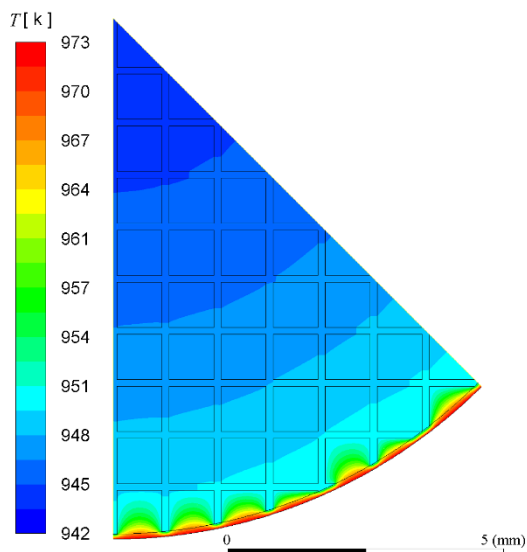
(c)

(d)

Fig. 7 (a) Variation of G_{gap}/G with thermal conductivity of the monolith substrate for different gas phase conductivities and gap thicknesses; Temperature distributions of the monolith reformer ($\delta = 0.1$ mm and $k_f = 0.1$ W/m·K) for the conditions without (b) and with (c) radiation heat transfer; (d) Variation of $G_{gap,rad}/G$ and G_{gap}/G with different wall temperatures.

Due to the high reforming temperature, the radiation heat transfer in the gap from the reactor wall to the monolith could play a role in improving the heat transfer near the wall. To account for this, the radiation model (DO model and S2S model) was added based on the simulations above with a gap thickness of 0.1 mm, k_s = 71 W/m·K and k_f = 0.1 W/m·K. Due to the close results generated by the two radiation models, only the results given by the DO model were shown in Fig.7. The temperature distributions for the conditions without and with the radiation heat transfer are shown in Fig. 7(b) and (c). Compared to the condition without a gap, a sharp temperature drop was observed near the outer wall for both the two conditions due to the obvious gap resistance mentioned above. Compared with the condition without consideration of radiation (shown in Fig.7 (b)), a lower temperature drop was achieved for the condition with radiation heat transfer (shown in Fig. 7(c)), which indicates an improvement of heat transfer by radiation near the wall gap. Higher center temperature (942 K) of the monolith reformer was also observed in Fig. 7(c) compared with that in Fig. 7(b) (944 K). The conditions with higher outer wall temperatures were also investigated as the results shown in Fig. 7(d). The values of $G_{gap,rad}/G$ and G_{gap}/G, with and without consideration of radiation, were calculated. Slight linear growth of the $G_{gap,rad}/G$ value and decrease of G_{gap}/G value were observed when the wall temperature was increased from 973 to 1173 K. The $G_{gap,rad}/G$ value was 12–19% higher than the G_{gap}/G value, which can be attributed to the positive effect of the radiation. However, the $G_{gap,rad}/G$ values are still not high (< 0.26) in any of the simulations, which indicates that the gap resistance was still the main source of radial heat resistance.
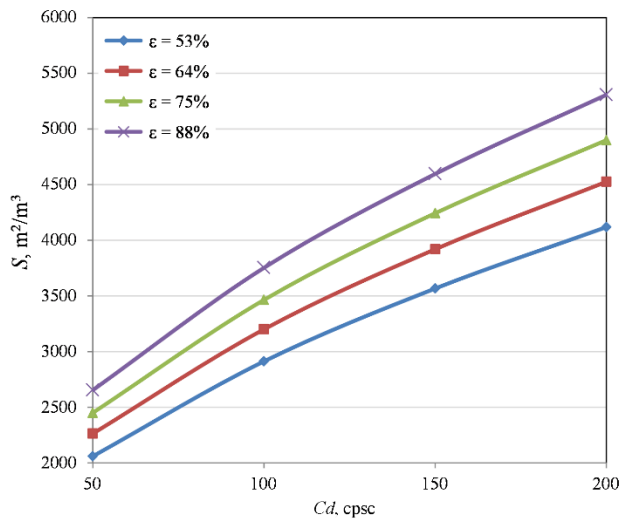
3.5 Selection of the geometric parameters

The design parameters regarding the radial heat transfer performance for a monolith reformer mainly consider three aspects: (1) geometric parameters (cell density (Cd), porosity (ε), diameter (d) and channel shape); (2) thermal conductivities of the monolith substrate, washcoat and gas phase (k_s, k_w and k_f,

respectively); (3) reaction heat of the catalytic SMR reactions, which are related to catalyst activity, thickness of washcoat, and reaction rates in the monolith channels. The aim of the design was to lower the cost of the materials (catalyst and monolith substrate), and optimize fabrication and energy consumption for heating and feed gas compression, while considering other constraints such as the volume limitations of the reformer. It is clear that optimization of the parameters discussed above are needed to achieve this aim.

In the present study, the influence of the geometric parameters (Cd, ε, and d) and thermal conductivity of monolith substrate (k_s) are illustrated by the optimization studies. Square channels were used, and other parameters were set as follows: k_{wash} = 1 W/m·K, k_f = 0.1 W/m·K, δ_{wash} = 30 μm, $Q_{wash,ref}$ = 3.6 × 10^4 kW/m³, ε = 0.53–0.88 and R = 10–80 mm. A simplified pseudo-homogenous 2-D model was used with the SMR reactions distributed throughout the whole solid geometry (Fig. 2(d)) instead of just in the monolith channels. The symmetric model was used for predictions of the effective thermal conductivity ($k_{r,eff}$) in the radial direction of the monolith reformers (by equation (14) and (15)), which showed good accuracy under the condition considering washcoat layer as discussed in section 3.3. The heat source S_R for the solid geometry was obtained by equation (8), and the average reaction heat per unit volume of the monolithic bed $Q_{mono,avg}$ was calculated by Q_m/V_{mono}, where Q_m is the heat transfer rate through the monolithic bed from the outer wall. The pseudo-homogenous model makes predictions possible for the quick evaluations of geometric parameters.

The amount of catalyst loaded onto the monolith substrates is mainly determined by the specific surface areas of the monoliths as well as the desired thickness of catalyst layer. Fig. 8(a) shows the specific surface areas of the monolith structures (S) with different porosities and cell densities provided by the CFD model. The surface area increased with an increase of porosity and cell density. The increment of

surface area is around 8–10% for adjacent porosities, while a 41.4% increase was obtained by doubling the cell density. The increase of the specific surface area results in a higher catalyst loading capacity per unit volume for the monoliths and consequently a higher reaction intensity. With respect to the endothermic SMR reactions, the reaction intensity was represented by $Q_{mono,avg}$. For monolith reformers with the same volume and under the same operating conditions, a higher value of $Q_{mono,avg}$ indicates a larger reforming capacity. In other words, a monolith reformer with a higher $Q_{mono,avg}$ could achieve the same reforming capacity as a larger device, which will decrease the space demands and lower the cost of the monolith substrate.
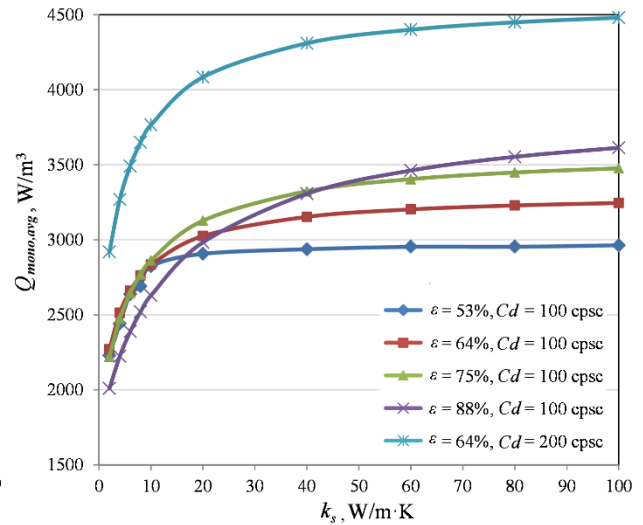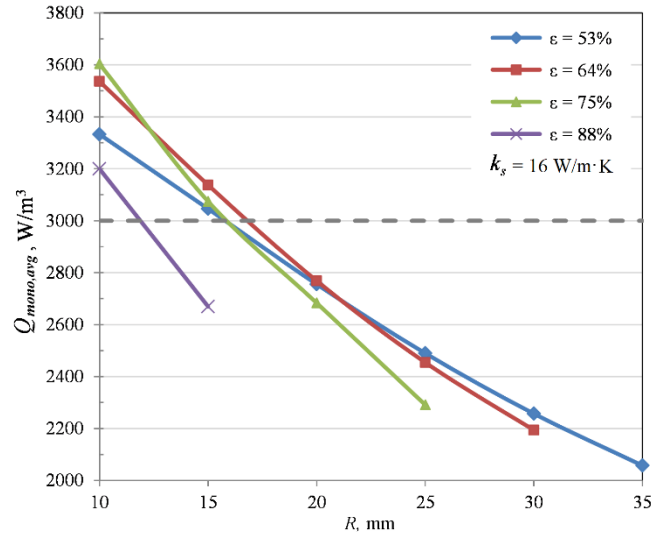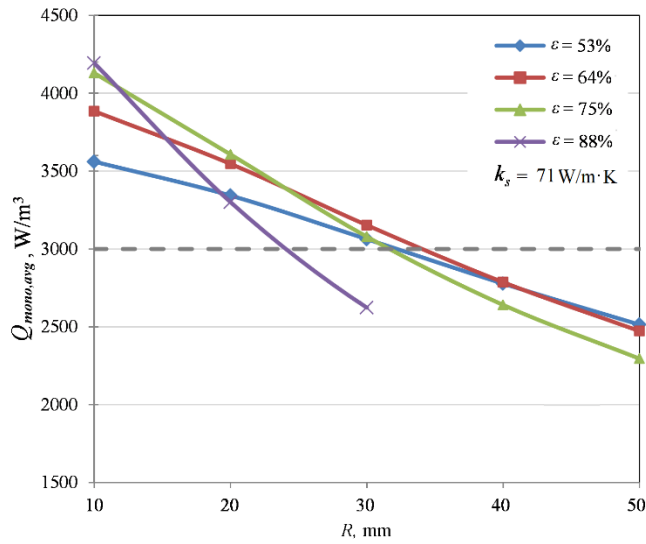

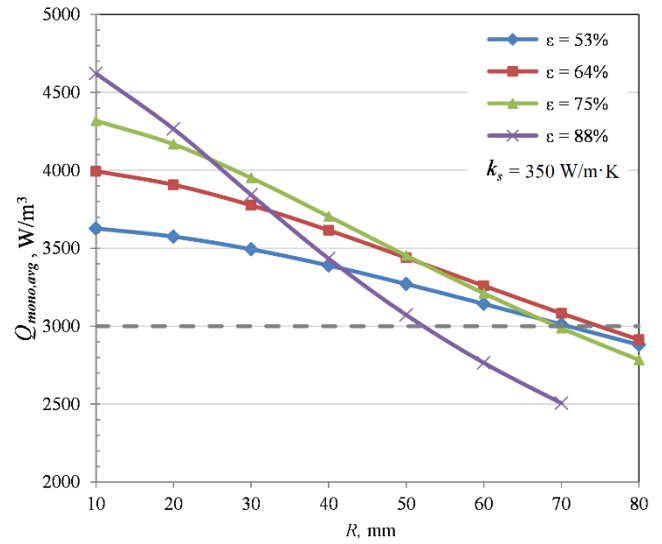(a)   (b)
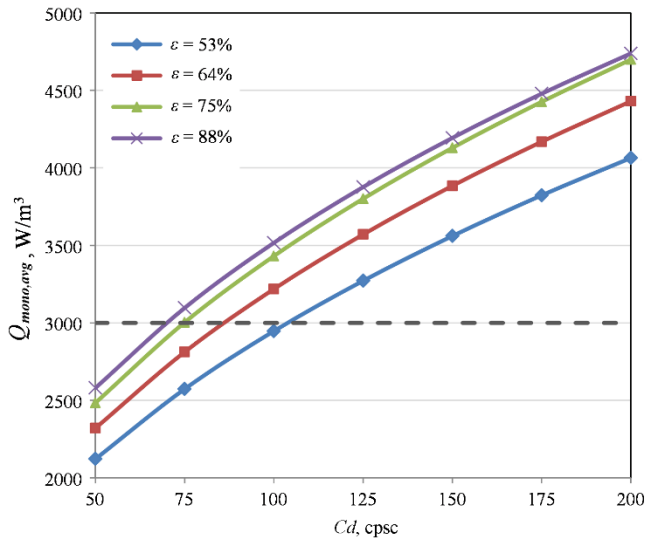
(c)

(d)

(e)

(f)

Fig. 8 (a) Specific surface areas of the monolith structures with different porosities, cell densities and R = 10 mm; (b) Variation of $Q_{mono,avg}$ with the thermal conductivity of the monolith substrate with various geometric parameters and R = 10 mm; (c) Variation of $Q_{mono,avg}$ with different cell densities and porosities, k_s = 71 W/m·K and R = 10 mm; Variation of $Q_{mono,avg}$ with the radius of monolith for Cd = 150 cpsc and (d) k_s = 16 W/m·K and. (e) k_s = 71 W/m·K and (f) k_s = 350 W/m·K.

Fig. 8(b) demonstrates the variation of $Q_{mono,avg}$ with the thermal conductivity of the monolith substrate with different geometric parameters. The $Q_{mono,avg}$ value increased with an increase cell density and in porosity (except $\varepsilon = 88\%$), which is consistent with the trend in Fig. 8(a). Significant decreases in the $Q_{mono,avg}$ values were noticed in the low k_s area, which can be attributed to the low effective thermal conductivity and very large temperature decrease (also see Fig. 5c) resulting in low reaction rates. The change of $Q_{mono,avg}$ values were much smaller for the condition with high k_s values, which indicates that the influence of heat resistance in the radial direction of a monolith reformer can be reduced by using a highly conductive monolith substrate such as nickel. Furthermore, Fig. 8(c) illustrates the variation of $Q_{mono,avg}$ with different cell densities and porosities for highly conductive monoliths ($k_s = 71$ W/m·K). The trend of $Q_{mono,avg}$ matches with that of the specific surface area in Fig. 8(a), which indicates that by using a highly conductive monolith substrate, the reforming capacity can be determined by the specific surface area of the monolith. In contrast, the influence of the radial heat resistance was not significant in these simulations. With a certain requirement of $Q_{mono,avg}$ value, the possible range of porosity and cell density can be obtained, as in Fig. 8(c). For instance, with a $Q_{mono,avg}$ value of 3000 kW/m^3 (dash line in Fig. 8(c)), the minimum required cell densities can be obtained for monoliths with different porosities between 75 and 125 cpsc.

By using a monolith substrate with a higher thermal conductivity, a larger diameter can be used for the design of monolith reformer (with the same ΔT_m value). Fig. 8(d) – (f) demonstrate the variation of $Q_{mono,avg}$ with the different radii of the monolith reformer for the three monolith substrates (FeCrAlloy, Ni and SiC with $k_s = 16$, 71 and 350 W/m·K respectively) reported in literatures with $\Delta T_m < 100$ K for all the simulations. The $Q_{mono,avg}$ decreased with an increase in radii, and this trend was more obvious for higher porosity monoliths (such as $\varepsilon = 88\%$) due to its low effective thermal conductivity. The maximum radius for a monolith reformer that can be obtained for a given required $Q_{mono,avg}$ can be met.

For instance, with $Q_{mono,avg}$ = 3000 kW/m³ (dashed line), in Fig. 8(e), the maximum radii values can be obtained for the monoliths, around 31–34 mm for ε = 53%, 64% and 75%, 24 mm for ε = 88%. These values are smaller for the FeCrAlloy based monoliths with around 15–17 mm for ε = 53%, 64% and 75%, 12 mm for ε = 88%, while larger maximum radii values were achieve for SiC based monolith with around 70–75 mm for ε = 53%, 64% and 75%, 53 mm for ε = 88%. These maximum radii values indicated that monolith reformer with a larger radius can be designed by using SiC based monolith substrate which is around 2 times and 4 times of those by using Ni and FeCrAlloy based monolith, respectively. In additions, the decreasing trend of $Q_{mono,avg}$ indicates that the increasing heat resistance and temperature difference in the radial direction will lower the efficiency of the catalyst near the center as well as the overall efficiency of the catalyst, e.g., in Fig. 8(d), when the radius was enlarged from 10 to 30 mm, the $Q_{mono,avg}$ value for the monolith with porosity ε = 53% decreased by 32%, while this decreases are 14% and 4% for the Ni and SiC based monoliths respectively.

4. Conclusion

The following conclusions can be drawn from the 2-D analysis of monolith reformers presented in this paper:

(1) Under the conditions without reactions, the symmetric and parallel models provided acceptable accuracy (<7% error) for the predictions of the effective radial thermal conductivity of the monolithic structures with square channels, while under the investigated conditions with the endothermic SMR reactions, the symmetric model provided acceptable accuracy (< 10% error) in moderate and high k_s area (k_s >10 W/m·K).

(2) The symmetric model also provided good accuracy for the conditions with the washcoat layer loaded on the monolith channels. Comparing with the CFD model without washcoat, the thermal influence of the washcoat layer is not significant for a highly conductive monolith reformer.

(3) The influence of radiation heat transfer in the monolith channels depends on the conductive heat transfer rate in the monolith. This influence is low for a highly conductive monolith reformer, whereas for the moderately conductive FeCralloy monolith, especially with high porosity and temperature, close attention should be paid to the radiation heat transfer. A simplified model has been developed to evaluate the importance of radiation for monolithic reformers.

(4) A wall gap as thin as 0.05 mm can significantly decrease the effective radial thermal conductivity of a highly conductive monolith reformer (e.g., with $k_s = 71$ W/m·K and $k_f = 0.3$ W/m·K, more than a 40% decrease of $k_{r,eff}$ was obtained) compared with the condition without a wall gap. Radiation heat transfer can improve the heat transfer in the gap to a limited degree. The variation of the gap resistance at different positions of the monolith reformer should also be considered for the evaluation of the effective thermal conductivities.

(5) A pseudo-homogenous 2-D model combined with the symmetric model has been developed for a quick evaluation of the geometric parameters for a monolith reformer. Monolith substrates with high conductivities (e.g., Ni and SiC) showed great potential in the intensification of the steam reforming process and reformer design.

The thermal analysis in the radial direction performed in this study can be combined with the analysis in the axial direction and used as the basis for further 3-D thermal analysis and optimization of monolith reformers.

Acknowledgement

References

[1] Rostrup-Nielsen JR, Bøgild Hansen J. Steam Reforming for fuel cells. In: Shekhawat D, Spivey JJ, Berry DA, editors. Fuel cells: technologies for fuel processing, Oxford: Elsevier; 2011, p. 50.

[2] Rostrup-Nielsen JR, Christiansen LJ. Concepts in syngas manufacture. London: Imperial College Press; 2011, p. 15, 85, 149.

[3] Dicks. AL, Pointon. KD, Siddle A. Intrinsic reaction kinetics of methane steam reforming on a nickel/zirconia anode. J Power Sources 2000; 86: 523–530.

[4] José Geraldo de Melo Furtado，George Cassani Gatti，Eduardo Torres Serra，Silvio Carlos Anibal de Almeida. Performance analysis of a 5 kW PEMFC with a natural gas reformer. Int J Hydrogen Energy 2010; 35: 9990–9995.

[5] Eugenio Calò, Antonella Giannini, Giulia Monteleone. Small stationary reformers for H2 production from hydrocarbons.. Int J Hydrogen Energy 2010; 35: 9828–9835.

[6] Stefania Specchia. Fuel processing activities at European level: A panoramic overview. Int J Hydrogen Energy 2014; 39: 17953–17968.

[7] Jung-Il Yang, Tae Wan Kim, Ji Chan Park, Tak-Hyoung Lim, Heon Jung, Dong Hyun Chun. Development of a stand-alone steam methane reformer for on-site hydrogen production. Int J Hydrogen Energy 2016; 41: 8176–8183.

[8] Vita A, Pino L, Cipiti F, Lagana M, Recupero V. Structured reactors as alternative to pellets catalyst for propane oxidative steam reforming. Int J Hydrogen Energy 2010; 35: 9810–9817.

[9] Kolb G. Fuel processing for fuel cells. Weinheim: Wiley-VCH; 2008, p. 217.

[10] Giroux T, Hwang S, Ruettinger W, Shore L. Monolithic structures as alternatives to particulate catalysts for the reforming of hydrocarbons for hydrogen generation. Appl Catal B 2005; 56: 95–110.

[11] Heck RM, Gulati RJ, Farrauto RJ. The application of monoliths for gas phase catalytic reactions. Chem Eng J 2001; 82: 149–156.

[12] Dai C, Lei Z, Zhang J, Li Y, Chen B. Monolith catalysts for the alkylation of benzene with propylene. Chem Eng Sci 2013; 100: 342–351.

[13] Cybulski A, Moulijn JA. Monoliths in heterogeneous catalysis. Catal Rev Sci Eng 1994; 36: 179–270.

[14] Tronconi E, Groppi G, Visconti CG. Structured catalysts for non-adiabatic applications. Curr Opin Chem Eng 2014; 5: 55–67.

[15] Flytzani-Stephanopoulos M, Voecks GE, Charng T. Modelling of heat transfer in non-adiabatic monolith reactors and experimental comparisons of metal monoliths with packed beds. Chem Eng Sci 1986; 41: 1203–12.

[16] Cybulski A, Moulijn JA. Modelling of heat transfer in metallic monoliths consisting of sinusoidal cells. Chem Eng Sci 1994; 49: 19–27.

[17] Groppi G, Tronconi E. Design of novel monolith catalyst supports for gas-solid reactions with heat exchange. Chem Eng Sci 2000; 55: 2161–71.

[18] Wu P, Li X, Ji S, Lang B, Habimana F, Li C. Steam reforming of methane to hydrogen over Ni-based metal monolith catalysts. Catal Today 2009; 146: 82–86.

[19] Fukuhara C, Yamamoto K, Makiyama Y, Kawasaki W, Watanabe R. A metal-honeycomb-type structured catalyst for steam reforming of methane Effect of preparation condition change on reforming performance. Appl Catal A Gen 2015; 492: 190–200.

[20] Katheria S, Deo G, Kunzru D. Washcoating of NiMgAl2O4 Catalyst on FeCralloy Monoliths for Steam Reforming of Methane. Energ Fuel 2017; 31: 3134–3153.

[21] Sharma PO, Abraham MA, Chattopadhyay S. Development of a Novel Metal Monolith Catalyst for Natural Gas Steam Reforming. Ind Eng Chem Res 2007; 46: 9053–60.

[22] Ryu J, Lee K, La H, Kim H, Yang J, Jung H. Ni catalyst wash-coated on metal monolith with enhanced heat-transfer capability for steam reforming SMR. J Power Sources 2007; 171: 499–505.

[23] Roh HS, Lee DK, Koo KY, Jung UH, Yoon WL. Natural gas steam reforming for hydrogen production over metal monolith catalyst with efficient heat-transfer. Int J Hydrogen Energy 2010; 35: 1613–9.

[24] Tables of Physical & Chemical Constants (16th edition 1995). 2.3.7 Thermal conductivities. Kaye & Laby Online. Version 1.0 2005; www.kayelaby.npl.co.uk.

[25] Hiramitsu Y, Demura M, Xu Y, Yoshida M, Hirano T. Catalytic properties of pure Ni honeycomb catalysts for methane steam reforming. Appl Catal A Gen 2015; 507: 162–168.

[26] Toshiyuki Hirano, Ya Xu. Catalytic properties of a pure Ni coil catalyst for methane steam reforming. Int J Hydrogen Energy 2017; 42: 30621–30629.

[27] Palma V, Ricca A, Meloni E, Martino M, Miccio M, Ciambelli P. Experimental and numerical investigations on structured catalysts for methane steam reforming intensification. J Clean Prod 2016; 111, Part A: 217–30.

[28] Chen J, Yang H, Wang N, Ring Z, Dabros T. Mathematical modeling of monolith catalysts and reactors for gas phase reactions. Appl Catal A Gen 2008; 345:1–11.

[29] Hayes RE, Rojas A, Mmbaga J. The effective thermal conductivity of monolith honeycomb structures. Cata Today 2009; 147 (SUPPL.): S113–S119.

[30] Schlereth D, Hinrichsen O. Comparison of a Pseudocontinuous, Heterogeneous 2D Conductive Monolith Reactor Model to a 3D Computational Fluid Dynamics Model. Ind Eng Chem Res 2014; 53: 11550–11556.

[31] Chenxi Cao, Nian Zhang, Yi Cheng. Numerical analysis on steam methane reforming in a plate microchannel reactor: Effect of washcoat properties. Int J Hydrogen Energy 2016; 41: 18921–18941.

[32] Nijhuis TA, Beers AEW, Vergunst T, Hoek I, Kapteijn F, Moulijn JA. Preparation of monolithic catalysts. Cat Rev Sci Eng 2001; 43: 345–380.

[33] Önsan ZI, Avci AK. Multiphase Catalytic Reactors Theory, Design, Manufacturing, and Applications. Hoboken, New Jersey: John Wiley & Sons; 2016, p. 173, 215.

[34] J.R. Welty, C.E. Wicks, R.E. Wilson. Fundamentals of Momentum, Heat, and Mass Transfer (5th ed.), Hoboken, New Jersey: John Wiley & Sons; 2008, p. 274.

[35] L. Leibowitz, R.A. Blomquist. Thermal Conductivity and thermal expansion of stainless steels D9 and HT9. Int J Thermophys 1988; 9: 873–883.

[36] R.W. Powell, R. P. Tye, M. J. Hickman. The thermal conductivity of nickel. Int J Heat Mass Transfer 1965; 8: 679–688.

[37] Rostrup-Nielsen JR, Rostrup-Nielsen T. Large-scale Hydrogen Production. Cattech 2002; 6: 150–159.

[38] Lao L, Aguirre A, Tran A, Wu Z, Durand H, Christofides PD. CFD modeling and control of a steam methane reforming reactor. Chem Eng Sci, 2016; 148: 78–92.

[39] M. Zeppieri, P.L. Villa, N. Verdone, M. Scarsella, P. De Filippis. Kinetic of methane steam reforming reaction over nickel- and rhodium-based catalysts. Appl Catal A Gen 2010; 387:147–154.

[40] S-T. Lee, R. Aris. On the effects of radiative heat transfer in monoliths. Chem. Eng. Sci. 1977; 32: 827–837.

[41] J. Sinkule, V. Hlaváček. Heat and mass transfer in monolithic honeycomb catalysts – III: radiation model. Chem. Eng. Sci. 1978; 33: 839–845

[42] R.E. Hayes, S.T. Kolaczkowski, W.J. Thomas. Finite-element model for a catalytic monolith reactor. Comput. Chem. Eng. 1992; 16: 645–657.

[43] A.L. Boehman. Radiation heat transfer in catalytic monoliths. AIChE J. 1998; 44: 2745–2755.

[44] P.M.Struk, J.S.T'ien, F.J.Miller, D.L.Dietrich. Transient numerical modeling of catalytic channels using a quasi-steady gas phase. Chem. Eng. Sci. 2014; 119:158–173.

[45] Niket S. Kaisare, Jay H. Lee, Andrei G. Fedorov. Hydrogen generation in a reverse-flow microreactor: 1. Model formulation and scaling. AICHE J 2005; 2254–2264.

[46] ANSYS Fluent Theory Guide, Release 18.0.

[47] Groppi G, Tronconi E. Continuous vs discrete models of nonadiabatic monolith catalysts. AICHE J 1996; 42: 2382–2387.

[48] Visconti CG, Groppi G, Tronconi E. Accurate prediction of the effective radial conductivity of highly conductive honeycomb monoliths with square channels. Chem Eng J 2013; 233: 224–230.

[49] Tronconi E, Groppi G, Boger T, Heibel A. Monolithic catalysts with 'high conductivity' honeycomb supports for gas/solid exothermic reactions: characterization of the heat-transfer properties. Chem Eng Sci 2004; 59: 4941–4949.

[50] Boger T, Heibel A. Heat Transfer in Conductive Monolith Structures, Chem Eng Sci 2005; 60: 1823–1835.

Appendix A

Radiation heat transfer in square channels and monoliths

Xiaoti Cui, Søren Knudsen Kær

Department of Energy Technology, Aalborg University, Pontoppidanstr. 111, 9220 Aalborg

1. Mathematical model

A single square channel was considered for further evaluation of the importance of radiation heat transfer in monolith structures. The lateral heat transfer in a square channel was illustrated in Fig. 1, where T_1 and T_2 are the temperature of the outer wall *A'* and *B'* respectively. The lateral heat transfer by both conduction along the wall and radiation in the channel occurs when $T_1 > T_2$. For a monolith structure, the scale of *L* and *d* in Fig. 1 are determined by the cell density *Cd*, porosity ε as well as the thickness of washcoat layer.
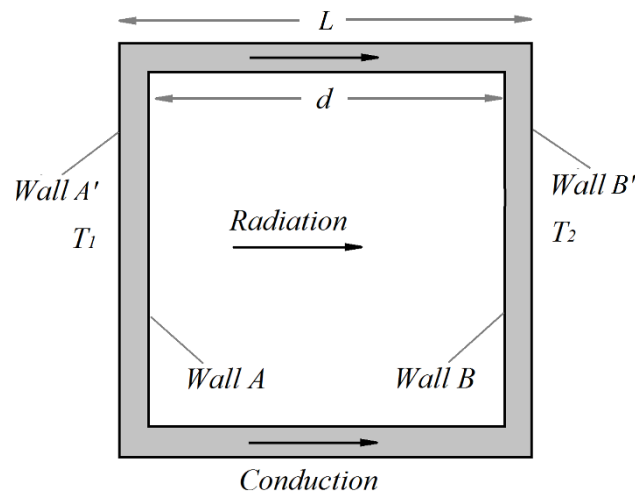

Fig. 1 The lateral heat transfer in a square channel.

CFD modeling has been conducted for the square channels from monolith structures with different porosities. The DO model was taken into account in the CFD model. Fig. 2(a) illustrates the radiation heat flux (heat flux from the wall surface is positive) in a square channel, where the net radiation heat fluxes for the upper wall and lower wall inside the channel were close to zero, the radiation heat mainly transferred from wall A to wall B.
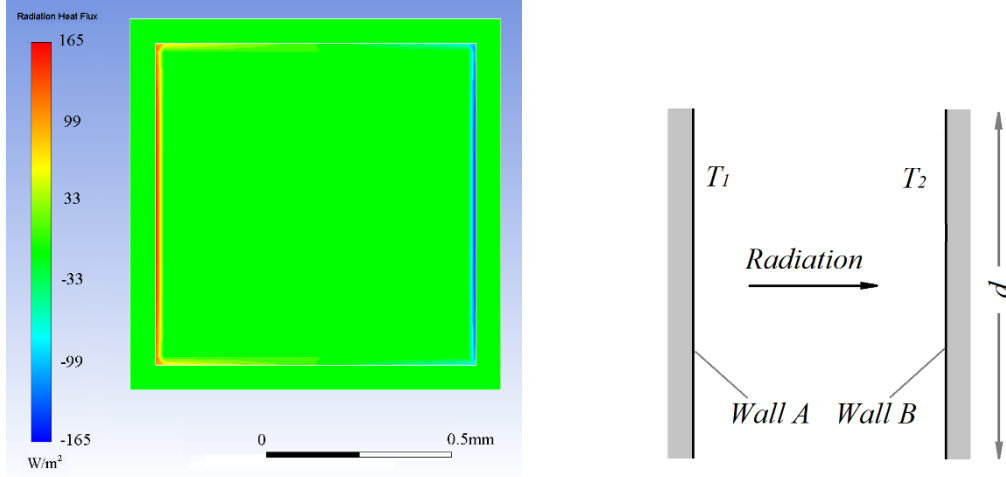
Fig. 2(a) The radiation heat flux in a square channel, $L = 1$ mm, $d = 0.866$ mm, $k_s = 16$ W/m·K, T_1=1173 K, $T_2 = 1172$ K; (b) radiation heat transfer between wall A and wall B.

For further simplification, the radiation heat transfer on the upper and lower wall inside the channel was not considered, and the temperature difference between the inner and outer wall (A and A' or B and B') of the channel was neglected. Only the radiation heat transfer between wall A and wall B was included as shown in Fig. 2(b). Assumed that wall A and B are gray surfaces, and the gas phase in the channel does not participate in the radiation heat transfer, the radiation heat flux from wall A to wall B can be expressed by [1]:

$$q_{rad} = \sigma \varepsilon^2 A F (T_1^4 - T_2^4) \tag{1}$$

where σ is the Stefan-Boltzmann constant (5.670×10^{-8} W/m²·K⁴), ε is the emissivity for the wall surfaces, A is the area (of wall A or B), F is the view factor, and $F = 1$ was set in the square enclosure according to the result of the CFD simulation mentioned above.

For the heat conduction in the channel wall, the conductive heat flux can be given by:

$$q_c = A k_{r,eff} \frac{\Delta T}{d} = A k_{r,eff} \frac{(T_1 - T_2)}{d} \tag{2}$$

where $k_{r,eff}$ is the effective thermal conductivity in the lateral direction of a square channel or the radial direction of a monolith structure which can be calculated by the symmetric model (equations

(12), (14) – (15) in the paper) for monolith channels. Combining equation (1) and (2), the enhancement factor f of the radiation heat transfer (mentioned in the paper, equation (19) in section 3.1) can be approximated by

$$f = \frac{q_{rad}}{q_c} = \frac{\sigma \varepsilon^2 d(T_1^2 + T_2^2)(T_1 + T_2)}{k_{r,eff}} \tag{3}$$

For a monolith reformer, the temperature near the outer wall of the monolith can be used for evaluating the importance of the radiation heat transfer. T_1 and T_2 were replaced by the outer wall temperature of the monolith T_w, then equation (3) can be simplified as

$$f = \frac{4\sigma \varepsilon^2 d T_w^3}{k_{r,eff}} \tag{4}$$

2. Comparison with CFD modeling

The simplified model (equation (4)) was compared with the CFD simulations for square channels (shown in Fig.1), and monoliths structures (shown in Fig. 2(a) and (c) in the paper) with and without SMR reactions. The dimensions of the square channels were determined by the geometry parameters of monoliths with the porosities of 0.53 – 0.88, cell density of 100 cpsc and radius of 9.9 mm. The outer wall temperature T_w is from 873 K to 1473 K. The thermal conductivities of 16 W/m·K and 71 W/m·K were chosen to represent the monolith substrates with moderate and high conductivities. The emissivity of 0.7 was set for the surface in the channels. $Q_{wash,ref} = 3.6 \times 10^7$ W/m³ was set for the condition with the SMR reactions.

The values of f calculated by the simplified model and the CFD simulations were shown in Fig. 3. Good agreement between the simplified model and the prediction by the CFD model for the square channels was noticed. The enhancement factor for the monoliths with and without the SMR reactions are lower than those for the square channels, the derivation is within 30% for most of the investigated

conditions. According to the investigations in the paper (section 3.3), the monoliths with the SMR reactions could provide a lower f value if a larger $Q_{wash,ref}$ value is set. The simplified model (equation (4)) can be used for evaluating the importance of the radiation heat transfer compared with the conductive heat transfer in the radial direction of monolithic reformers.
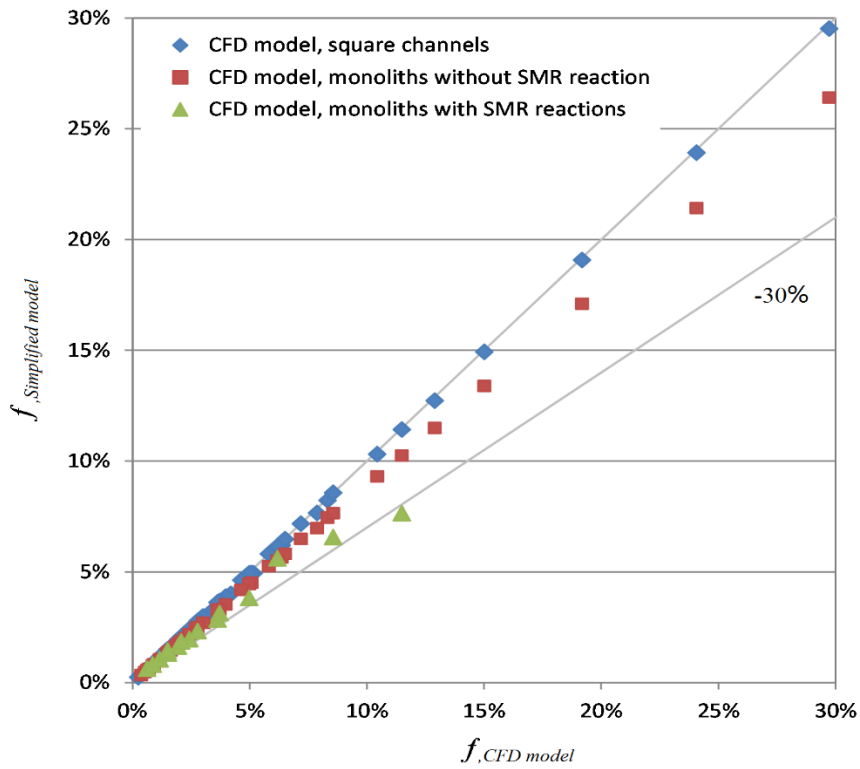

Fig. 3 The enhancement factor f calculated by the simplified model and the CFD model.

Reference

[1] Gregory Nellis, Sanford Klein. Heat transfer. Cambridge: Cambridge University Press; 2009, p. 1045.